NJC

PAPER

View Article Online
View Journal | View Issue

Cite this: *New J. Chem.*, 2017, **41**, 7356

Synthesis of cobalt ferrite nanoparticles by constant pH co-precipitation and their high catalytic activity in CO oxidation†

Jasmine Thomas,[ab] Nygil Thomas, *[b] Frank Girgsdies, [c] Malte Beherns, [d] Xing Huang, [c] V. D. Sudheesh [e] and Varkey Sebastian[e]

Received 17th February 2017,
Accepted 8th June 2017

DOI: 10.1039/c7nj00558j

rsc.li/njc

A series of cobalt ferrite samples were synthesized from a metal nitrate solution at constant pH between 9 and 12 by the controlled co-precipitation method without any surfactant. Cobalt and iron nitrates and sodium hydroxide base were simultaneously dosed so that the pH was precisely controlled during co-precipitation. The samples were characterized by PXRD, SEM, TEM, BET, and TPR. Careful analysis of typical PXRD peak profiles suggested the presence of two different variants of cobalt ferrite, a nano-scale material giving rise to broad peak tails and a more crystalline material leading to a sharper central profile. Rietveld refinement could be used to quantify the relative amount of both nano and crystalline fractions in these samples indicating that their relative abundance can be controlled by the co-precipitation pH. TEM analysis further proved the presence of both crystalline and nanocrystalline region in the samples. The average crystallite size of the cobalt ferrite nanocrystallites was 4–5 nm. These samples exhibit high BET surface area, in the order of 200 m^2 g^{-1}. The samples were tested for catalytic performance in the CO oxidation reaction. The surface area, reduction behavior, and catalytic performance of ferrites were dependent on the relative amount of both the crystalline and nanocrystalline phases.

Introduction

Nanomaterials are of great importance because of their special properties compared to bulk materials. Depending on the size, shape and surface morphology, nanomaterials can show different electrical, optical, and catalytic properties. The catalytic activity of nanomaterials is related to the high surface area and large surface to volume ratio. Ferrite nanoparticles of general formula AFe_2O_4 in which the divalent A^{2+} and Fe^{3+} ions distributed in T_d and O_h sites of the cubic spinel structure are good candidates for oxidation catalysts since their catalytic activity can be easily modified by changing the cation distribution.[1–5] Cobalt ferrite is an important candidate in the spinel family and was studied extensively due to its interesting magnetic properties such as high saturation magnetization (M_S), coercivity (H_C), and magnetocrystalline anisotropy.[6,7] Due to its remarkable chemical stability, mechanical hardness and high activity, it is also interesting as an oxidation catalyst.[8–11]

A number of chemical methods such as co-precipitation,[12,13] sol–gel,[14] hydrothermal,[15] micro-emulsion,[16,17] spray pyrolysis,[18] reverse micelles,[13] sonochemical,[19] and organic precursor decomposition[20] are available for the synthesis of ferrite nanoparticles. It was generally found that the size and shape and the physical properties of nanoparticles prepared using these techniques are highly dependent on the method of synthesis and the nature of the surfactant used. The reaction temperature, pH of the medium, annealing temperature, ageing time, and concentration of the reactants are some of the important parameters that influence the size, shape, and physical properties of the nanoparticles. The co-precipitation method is a widely used method in nanoparticles synthesis owing to advantages such as low cost, environmentally benign method, easy tuning of the microstructure, and high reproducibility. The co-precipitation method involves nucleation followed by growth of the particles which are strongly affected by the conditions of the precipitation reactions.[21]

Templeton *et al.* prepared cobalt ferrite samples by precipitation from a solution consisting of $FeCl_2$, and $Co(NO_3)_2$ using ammonium hydroxide as a precipitating agent.[22] They investigated the effects of pH, precipitation temperature, and agitation on the morphology of the particles formed. Rajendran *et al.* used mixed aqueous solutions of iron and cobalt in the concentration range of

[a] *Department of Chemistry, S N College, Kannur, Kerala, India*
[b] *Department of Chemistry, Nirmalagiri College, Nirmalagiri, Kannur, Kerala, India. E-mail: nygill@gmail.com*
[c] *Department of Inorganic Chemistry, Fritz-Haber-Institut der Max-Planck-Gesellschaft, Faradayweg 4-6, 14195 Berlin, Germany*
[d] *University of Duisburg-Essen, Faculty of Chemistry and Center for Nano integration Duisburg-Essen (CENIDE), Universitätsstrasse 7, 45141 Essen, Germany*
[e] *Department of Physics, Nirmalagiri College, Nirmalagiri, Kannur, Kerala, India*
† Electronic supplementary information (ESI) available. See DOI: 10.1039/c7nj00558j

0.1–1.0 M such that $[Co^{2+}]:[Fe^{3+}] = 1:2$, followed by oxidation under controlled conditions using NaOH and H_2O_2.[23] Kim *et al.* have prepared $CoFe_2O_4$ nanoparticles in aqueous solutions at various temperatures using the co-precipitation approach without using a template.[24] When the precipitation temperature varied from 20 to 80 °C the average particle sizes were increased. Houshiar *et al.* compared the effect of different preparation methods like combustion, co-precipitation, and precipitation on the structural and magnetic properties.[12] Ayappan *et al.* investigated the effect of digestion time on the crystallite size, cation distribution, and magnetic properties of $CoFe_2O_4$ nanoparticles synthesized by the co-precipitation method.[25] Fannin *et al.* compared the microwave absorbent properties of cobalt ferrite powders prepared by co-precipitation and subjected them to different thermal treatments.[26] Gul *et al.* compared the optical, magnetic, and electrical investigation of cobalt ferrite nanoparticles synthesized by the co-precipitation route.[27] Zhang *et al.* compared the composition and magnetic properties of cobalt ferrite nanoparticles prepared by the co-precipitation method.[28] Maaz *et al.* synthesized cobalt ferrite using a wet chemical method using oleic acid as the surfactant.[29]

Although there are many reports on the preparation of cobalt ferrite nanoparticles by the co-precipitation method, only few address the relationship of synthesis parameters, in particular pH and micro-structure with catalytic properties in heterogeneous oxidation reactions. In addition, most of the reported studies concentrate on bringing the pH value to a desired value at the end of precipitation, rather than maintaining the pH constant from the beginning of the precipitation. In a typical procedure, the pH was brought to the desired value by either adding a certain amount of base to the metal nitrate solution or *vice versa* similar to a titration experiment interrupted at a given pH. As a consequence, samples synthesized at different pH values will all follow a similar titration-curve like pH evolution making it sometimes difficult to identify differences between the samples and to clearly trace these differences back to the precipitation conditions. The present study reports the synthesis of cobalt ferrite nanoparticles using the co-precipitation method, keeping the pH better controlled and constant by simultaneous dosing. This method is usually more reproducible and more scalable and often applied in industry. In an academic study like this one, better defined differences between materials co-precipitated at different pH can be expected giving rise to a clearer correlation of this synthesis parameter with structural and catalytic properties. This constant pH co-precipitation method was successfully employed for example to prepare methanol synthesis catalysts.[30] However, to the best of our knowledge, this is the first time this approach is being used for the synthesis of cobalt ferrite spinel nanoparticles. The resultant materials were used as catalysts in the CO oxidation reaction.

Experimental methods

Synthesis

A constant pH co-precipitation method was used for the synthesis of cobalt ferrite nanoparticles. A computer-controlled Mettler-Toledo Labmax setup was used to obtain stringent control over the pH, flow rate of solutions, ageing time, and temperature during the preparation of the samples. 250 ml of 0.1 M iron nitrate ($Fe(NO_3)_3{\cdot}9H_2O$) and 250 ml of 0.05 M cobalt nitrate ($Co(NO_3)_2{\cdot}6H_2O$) were mixed. The precipitating agent was 0.8 M NaOH. Here the precipitating agent and the metal salt solutions were dosed simultaneously into a reactor containing 400 ml of bi-distilled water within 40 min. The temperature was kept at 60 °C *via* a constant flow of heated/cooled oil flowing through the double-wall of the reactor. The dosing of the mixed metal nitrate solution was conducted at a constant rate and the addition of the base was controlled in a way that the pH of the resulting solution was kept constant. A series of samples was prepared at pH 12, 11, 10 and 9, respectively. The solids were aged for 2 h at 60 °C under stirring in the mother liquor without pH control. The products were filtered and washed with micro pore water until the conductivity of the filtrate was less than 1 mS cm^{-1}. The mixture was centrifuged and dried overnight at 110 °C. The sample prepared at pH 11 was calcined at 190, 300, 500, and 600 °C in air using a temperature ramp of 2 °C min^{-1} and a hold time of 120 min.

Characterization

The crystalline nature of the samples was studied using two Bruker AXS D8 Advance diffractometers in Bragg–Brentano geometry, using Cu $K\alpha_{1+2}$ radiation (Advance Series II: secondary graphite monochromator and scintillation detector; Advance DaVinci: Ni filter and Lynx Eye energy dispersive position sensitive silicon strip detector). The reference patterns for comparing the X-ray diffraction pattern of the nanoparticles were taken from the PDF (Powder Diffraction File)-database issued by the ICDD (International Centre for Diffraction Data). Thermogravimetric analysis (TGA) was performed on a Netzsch STA449 thermo balance connected to a quadrupole mass spectrometer (Thermo Star, Pfeiffer). The measurements were performed with approximately 15 mg sample in a temperature range of 30–1000 °C with a rate of 5 kpm under controlled gas flow (21% O_2 in Ar, 100 ml min^{-1}). The surface morphology of the samples was studied using a Scanning Electron Microscope (SEM) Hitachi S-4800 (FEG) equipped with a field emission gun. The samples were loosely dispersed on conductive carbon tape. The SEM was operated at low accelerating voltage (1.5 kV) for a better resolution of the surface features of the samples. Elemental analysis by using X-ray energy dispersive spectroscopy (EDX) was carried out at 15 kV using an EDAX detector connected to the SEM. HRTEM images were taken on a FEI Titan 80-300 equipped with a Cs corrector at 300 kV. The surface area of the samples was determined by N_2 physisorption (Quantachrome Autosorb-1) using the BET method. The samples were degassed for 2 h under dynamic vacuum conditions at 80 °C. The pore size distribution was determined from the desorption branches of the isotherm using the BJH method. The reduction patterns of the samples were studied using temperature programmed reduction (TPR). 30 mg of the calcined sample was reduced in 5% H_2 in Ar at a heating rate of 6 °C min^{-1} (80 mL min^{-1}) in a fixed bed reactor (TPDRO-1100, CE instruments). The H_2

consumption was monitored using a thermal conductivity detector (TCD).

Catalytic testing

CO-oxidation as a catalytic test reaction was carried out in a self-constructed catalytic reactor setup which is equipped with an on-line gas analyzer (X-Stream, Emerson/Rosemount), consisting of a paramagnetic sensor and an infrared detector to quantify O_2, CO, CO_2, and H_2O. The temperature in the catalyst bed can be directly monitored by an analog connection to the gas analyzer. The setup is equipped with a switch-board for mixing the carrier gas (He 5.0) with CO (3.7), O_2 (5.0), or H_2 (5.0) with the help of 6-port switching valves (Valco, Vici). Every gas line is equipped with a filter, a mass-flow controller (E1-flow, Bronkhorst), a check valve, and a shut-off valve. The CO-gas line is equipped with a carbonyl remover, consisting of a tube filled with inert SiC and heated to 573 K. The carrier gas line is equipped with a water and oxygen filter. The reactor itself is a U-tube reactor with an inner diameter of 5 mm, made of glass-lined steel (SGE). It is placed inside a Cu-block oven for a maximum temperature of about 773 K, controlled by a Watlow thermo-controller unit and offering an isothermal zone of about 4 cm (±1 K). The oven is equipped with a pressured-air connection to make faster cooling possible. Usually, 25 mg of the catalyst, diluted by 250 mg of inert SiC (particle diameter: 250–355 μm) were weighed out and reduced in 5% H_2–He or in 2% CO–He (100 ml min^{-1}) at different temperatures (2 kpm, holding time 30 min). For the succeeding CO-oxidation, normally three repeated light-off conversion cycles were measured (100 ml min^{-1}, 0.5% O_2, 1% CO, 98.5% He) from 323 to 523 K (2 kpm heating rate, 15 min holding).

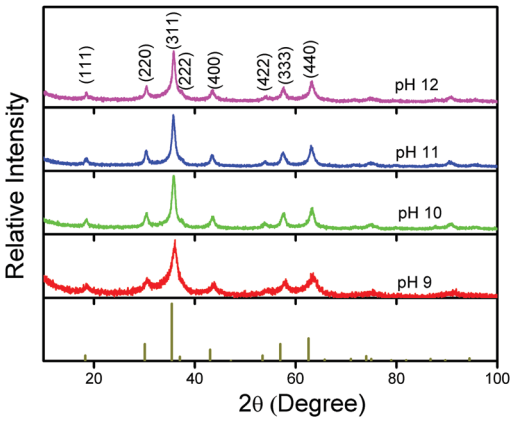

Fig. 1 PXRD patterns of cobalt ferrite synthesized at different pH at 60 °C.

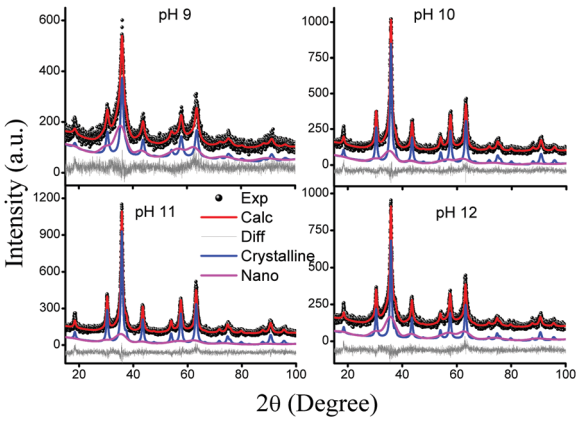

Fig. 2 Rietveld-refined PXRD pattern of the samples.

Results and discussion

All samples were prepared by co-precipitation of a Co^{2+}/Fe^{3+} nitrate solution with a basic solution of NaOH as the precipitating agent at constant pH and at a temperature of 60 °C. This constant pH synthesis method has been used for the successful preparation of a number of inorganic compounds.[31,32] The experimental set up is capable of monitoring the dosing rate, pH, reaction temperature, turbidity *etc.* A schematic diagram of the set up is shown in ESI† (Fig. S1). The variation of pH during the synthesis is shown in ESI,† Fig. S2, which shows only minor pH oscillations during co-precipitation and no abrupt pH changes during ageing. It can be concluded that fine control over the pH can be achieved by this method.

The PXRD pattern of the samples synthesized at different pH values are shown in Fig. 1. The 111, 220, 311, 222, 400, 422, 333 and 440 peaks, obtained by indexing the PXRD patterns assuming a cubic lattice, match well with that of spinel type cobalt ferrite structure. No indication for crystalline impurity phases was observed. A whole powder pattern fit according to the Rietveld method confirms the presence of a spinel type oxide, but also reveals that the observed peaks show a deviation from the usual Lorentzian shape. Firstly, they have a tendency towards a super-Lorentzian shape (*i.e.* sharp tips combined with broader tails), which is often an indication of a broad, possibly multi-modal crystallite size distribution. Secondly, the base of the peaks, especially at the lower angle side, exhibits some asymmetry which is not due to instrumental contribution, but due to an inhomogeneous distribution of the lattice parameter. To approximate and parameterize these effects, a second cobalt ferrite phase was added to the refinement model. The refined patterns in Fig. 2 show that upon the addition of the second phase, the experimental patterns can be refined in a satisfactory manner without substantial deviation of the calculated and measured data. Selected parameters obtained from the refinement are given in Table 1. With this approach, the patterns are simulated by a more crystalline component with narrower peaks and a less crystalline or nanocrystalline component with substantial peak broadening. The nanocrystalline component representing the broad bases of the peaks yields higher lattice parameters (shift to lower angles) than the crystalline contribution forming the peak tips. As the diffraction-based domain sizes for the nanocrystalline form are in the range of 2 nm, we assume that the lattice parameter deviation can be attributed to a crystallite size effect, which results from the different energies of the surface compared to the bulk atoms. Anyway it should be pointed out that the two-phase model is only a simple approximation to a real size- and lattice parameter distribution of unknown nature.

Table 1 The parameters extracted from the Rietveld refinement data for the samples synthesized at different pH

pH	% of nano crystalline phase	Lattice parameter (Å)		Crystallite size (nm)	
		Nano crystalline	Crystalline	Nano crystalline	Crystalline
9	49	8.413(9)	8.2790(3)	2	7
10	27	8.463(11)	8.3225(11)	2	11
11	24	8.424(11)	8.3316(10)	2	11
12	47	8.385(5)	8.3263(13)	2	12

Table 2 The parameters extracted from the Rietveld refinement for the samples synthesized at pH 11 calcined at different temperatures

Calcination temperature (°C)	% of nano crystalline phase	Lattice parameter a (Å)		Crystallite size (nm)	
		Nano crystalline	Crystalline	Nano crystalline	Crystalline
190	27	8.392(6)	8.3279(6)	2	12
300	24	8.412(6)	8.3222(6)	2	12
500	5	8.460(2)	8.3630(3)	3	15
600	—	—	8.3782(2)	—	22

Thus, the parameters resulting from the fits should not be expected to be precise. Still, they can be used to reveal trends in the evolution of the crystallite sizes with variation of the synthesis parameters.

By comparing the results of the PXRD measurements at different constant pH values, one can conclude that the crystallinity of the samples is dependent on the pH at which the sample is prepared. The Rietveld refinement reveals that in all samples, a combination of crystalline and nanocrystalline phases is present but their ratio is different at different pH values. Crystalline phase formation increases upon increasing the pH up to 11 but further increase to 12 causes a reverse effect. Also, in the nanocrystalline form, the lattice parameter decreases with increasing pH.

To get a better understanding of nanocrystalline and crystalline phase formation, the sample prepared at pH 11 was subjected to heat treatment at different temperatures. From the PXRD patterns of the calcined samples, it is clear that the crystallinity of the sample increases with an increase in calcination temperature (Fig. 3). The nanocrystalline phase, upon calcination, sinters likely by particle coalescence and forms larger-sized, more crystalline particles. The structural parameters of the calcined samples are shown in Table 2. The crystalline form of the as-prepared samples has a lower value of lattice parameter compared to that reported in the literature. Upon increase of the calcination temperature, an increase in lattice parameter is observed. The sample calcined at 500 °C shows a very faint nanocrystalline component. Hence the lattice parameter and crystallite size of this component may be unreliable. The sample calcined at 600 °C did not show any nanocrystalline component, whose lattice parameter is very close to that of bulk cobalt ferrite. In other words, the 600 °C calcined sample exhibits more homogeneous distribution which can be fitted with a single peak as a result of sintering and possibly cation re-distribution.

Fig. 4 shows the SEM images of cobalt ferrite samples synthesized at different constant pH. The materials consist of fine particles, which are hard to resolve in SEM in agreement with the small domain sizes found by PXRD. These particles form porous aggregates and seem to be finer in case of the sample precipitated at pH 9 in accordance with the higher fraction of nano-crystalline component in this sample. The average SEM-EDX analysis shows that the relative cation At% is in the ratio of 1:2 which is in good agreement with the atomic percentage in cobalt ferrite (ESI,† Table S1).

The SEM images of the calcined samples (Fig. 5) clearly indicate that the crystallite size increases with increase in calcination temperature. This result also matches well with the PXRD analysis of the calcined samples. The particle morphology was changed to more and more roundish shape. At 600 °C the particle size is in good agreement with the domain size determined by Rietveld refinement of approximately 20 nm as the nanocrystalline portions have vanished.

Fig. 6 shows representative TEM images of the sample synthesized at pH 9. Fig. 6a shows an overview at moderate magnification. It can be clearly seen that the sample consist of both bigger crystallites and lots of smaller ones as well. Fig. 6b shows an image at increased magnification and two spots have

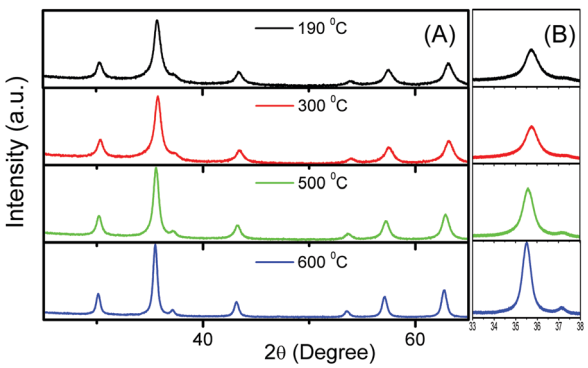

Fig. 3 PXRD pattern of the sample prepared at pH 11 after different calcinations (A). Enlarged view of (311) peaks (B).

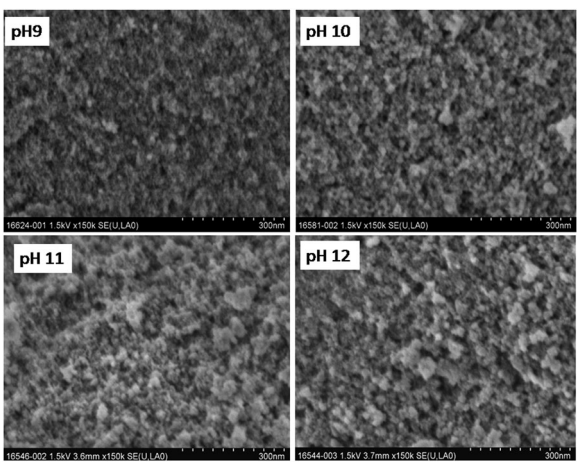

Fig. 4 SEM images of the samples at different pH.

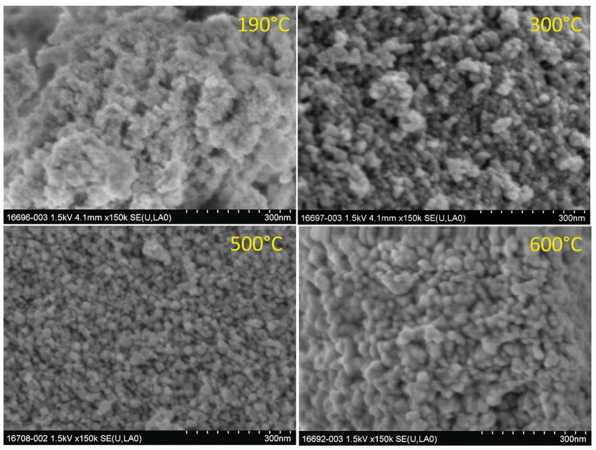

Fig. 5 SEM images of the sample prepared at pH 11 after different calcinations.

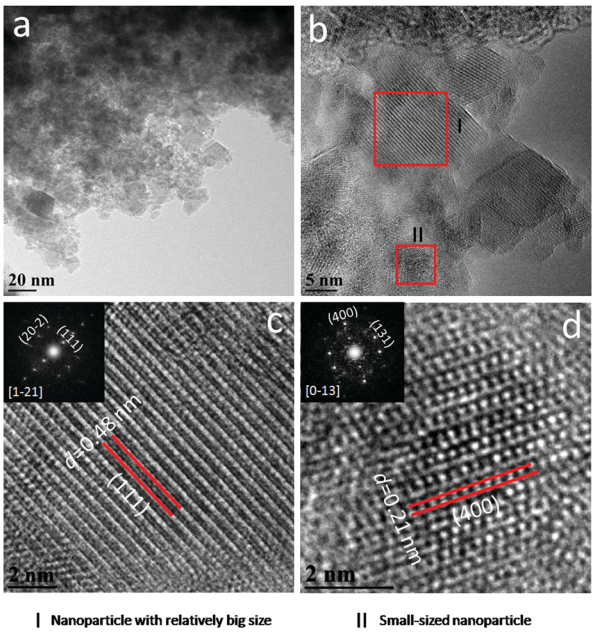

Fig. 6 TEM images of the sample prepared at pH 9 (inset corresponding SAED pattern).

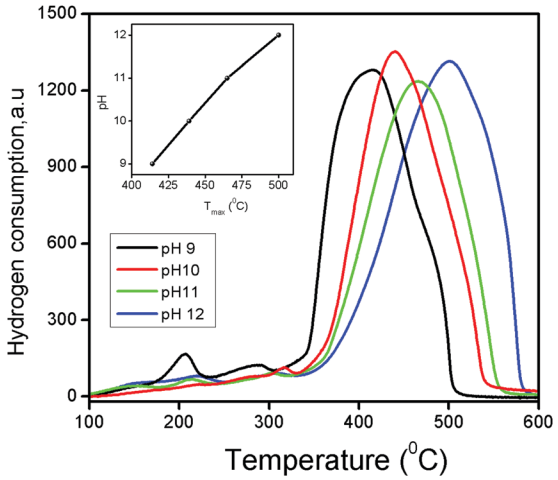

Fig. 7 TPR profile of the samples synthesized at different pH.

been identified from this region and images obtained at atomic resolution and are shown in Fig. 6c and d. Fourier transforms of the corresponding images are shown as insets. The patterns confirm the presence of cubic spinel. From Fig. 6c and d the lattice spacing of the (*hkl*) plane (111) and (400) respectively was obtained. The lattice parameter obtained using the corresponding lattice spacing calculation gives 8.31 Å as lattice parameter corresponding to crystalline area and 8.40 Å corresponding to nanocrystalline area. The results obtained are very close to the values obtained from Rietveld refinement for the sample prepared at pH 9. The clarity and contrast of the Fourier transforms also indicate the difference between crystalline and nanocrystalline phase. Hence the TEM images confirm the results obtained from PXRD and SEM.

Fig. 7 shows the TPR profiles of the samples synthesized at different pH. It can be seen that there is one predominant reduction peak for all the samples when the oxide is reduced to the metals. The pH 9 sample shows a T_{max} of this feature of 410 °C. The onset temperature is ~320 °C. All profiles have similar shape but the temperature maximum (T_{max}) is shifted to higher temperature with increasing pH, while the onset temperature remains similar. Interestingly, the T_{max} is directly proportional to the pH of the reaction, *i.e.* the complete reduction occurs at higher temperature as the pH increases. There is a significant difference in T_{max} of nearly 100 °C between the samples synthesized at pH 9 and 12. The relative amount of nanocrystalline phase in the pH 9 sample is higher compared to that in other samples.[33,34] Reducing the nanocrystalline domains is expected to be easier compared to crystalline domains. However, this trend is not reflected in the last sample synthesized at pH 12. This may be due to the larger size of the crystalline phase in this sample compared to other samples which might lead to a higher T_{max}.

The presence of additional peaks at low temperature and the asymmetric profile indicate that in these samples, there is a superposition of various reduction transformations taking place simultaneously. This prevents us from drawing a clear boundary between each reduction step and makes the exact explanation of the phenomenon difficult. In addition, there are many parameters like composition, method of preparation, reducing gas, *etc.* which influence the reducibility of the samples. Due to the broad patterns, the elementary steps of Fe^{3+} and Co^{2+} reduction cannot be distinguished from the TPR curves.[35] The literature suggests that the more easily reducible cations (in this case Co^{2+}) promote the reduction of iron cations which gets subsequently reduced.[34] In the case of spinels the reduction of Fe^{3+} which is present in both octahedral and tetrahedral sites to metallic Fe^0 occurs relatively at a much lower temperature compared to Fe_2O_3 probably due to spillover effect.[36] Co^{2+} cation is reduced by hydrogen to the corresponding metal which "dissociates and activates the hydrogen" for reduction of the trivalent cation Fe^{3+} indicating that the

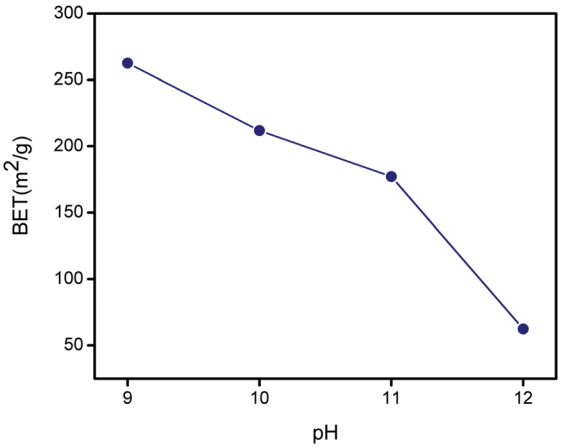

Fig. 8 BET surface area of the samples at different pH.

presence of cobalt makes the iron easier to reduce. There is also another explanation that reduction of cations from octahedral sites takes place first, followed by the reduction of the cations from tetrahedral sites.[37] The relative intensity of the peaks is different for different samples and shows that there is no clear demarcation between these processes.

Fig. 8 shows the relation of BET surface area with pH. Co-precipitation method gives exceptionally high surface area compared to other synthesis methods. Among these, the sample synthesized at pH 9 has a significantly higher surface area compared to others. The present value, 263 $m^2\ g^{-1}$ for pH 9 sample is one of the highest surface area value reported in the literature for a co-precipitated sample.[23,38] This may be due to the high amount of nanocrystalline phase in the pH 9 sample. The pH 12 sample shows much lower surface area and deviates from the rest of the samples.

Fig. 9 shows the N_2 adsorption–desorption isotherms of $CoFe_2O_4$. Mesoporosity of the samples is confirmed by the appearance of a hysteresis. Samples synthesized at pH 9, 10, and 11 (Fig. 4) show the type IV and V shape which is typical for mesoporous adsorbents materials.[39–42] The shapes suggest that

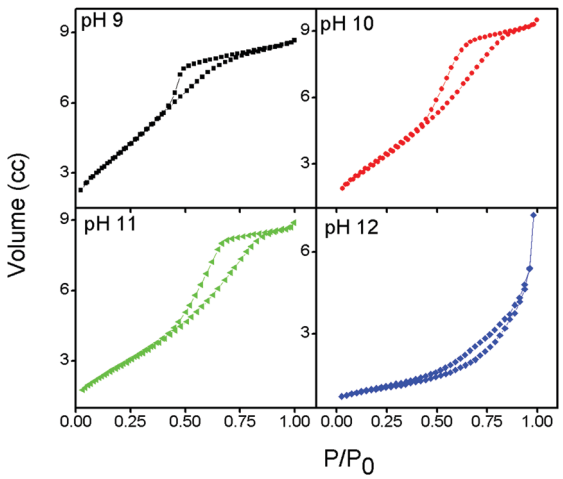

Fig. 9 N_2 adsorption–desorption isotherms of $CoFe_2O_4$.

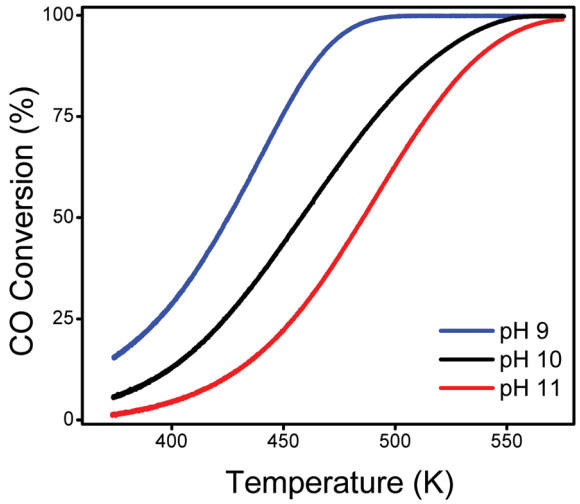

Fig. 10 CO conversion activity of the samples synthesized at pH 9, 10, and 11.

the hysteresis exhibited by these samples belong to the types H2(a) and H2(b) which has a triangular shape. Many inorganic oxides exhibit H2-like hysteresis loops, suggesting that the distribution of pore size and shape is not well defined. This hysteresis is due to the presence of ink-bottle type pores which has smaller entrance and wide body. The sample synthesized at pH 12 shows the hysteresis of type H3 which does not exhibit any limiting adsorption at high p/p_0. This type is observed for aggregates of plate-like particles giving rise to slit-shaped pores.[42]

The catalytic activity of cobalt ferrite synthesized at different pH was studied in CO oxidation reaction. The samples studied are the ones synthesized at pH 9, 10 and 11, for which a clear trend in many properties has been observed. The CO oxidation reaction was investigated at atmospheric pressure and runs up to 4–5 temperature cycles. There was a slight decrease in the activity of the first cycle compared to the remaining cycles. From the second cycle activity remains the same. Fig. 10 shows the CO oxidation activity of the second cycle for pH 9, 10, and 11. Catalytic activity strongly varied between the three samples. 50% conversion was reached for the pH 9 sample at T_{50} = 427 K and for the pH 11 sample at T_{50} = 487 K. The pH 10 sample achieved 50% conversion at 458 K, which is in between pH 9 and 11. 100% conversion was achieved for the pH 9 sample at 490 K and at 569 K for pH 11. In particular, it is seen that cobalt ferrite synthesized at pH 9 was active at room temperature, while cobalt ferrite synthesized at pH 11 was not. The sample synthesized at pH 9 exhibits a higher specific surface area and a higher content of the nanocrystalline phase. From the catalytical data it can be seen that as the content of the nanocrystalline phase increases the activity also increases. A brief comparison of the CO oxidation activity of oxide based solid powder catalysts is given in Table 3. From the table it can be concluded that the present catalysts are much more active for CO oxidation compared to the reported values so far.

Table 3 Comparison of CO oxidation activity for various catalyst

Material	Temperature (K) 100/90% conversion ($T_{90/100/50/44}$)	Reference
Fe_2O_3, CeO_2	>700	Bao *et al.*[48]
Fe_2O_3–CeO_2	>500	Bao *et al.*[48]
$Co_{0.9}Fe_{2.1}O_4$ film	503	Kouotou *et al.*[49]
α-Fe_2O_3	657 (T_{90})	Kouotou *et al.*[49]
$CoFe_2O_4$	533 (T_{90})	Tian *et al.*[50]
$Co_{0.9}Fe_{2.1}O_4$	503	Kouotou *et al.*[51]
$Co_{1.8}Fe_{1.2}O_4$	523	Kouotou *et al.*[51]
$Co_{2.1}Fe_{0.9}O_4$	571	Kouotou *et al.*[51]
$Co_{0.32}Fe_{0.16}O_{0.52}$	>723	Lee *et al.*[52]
$CuFe_2O_4$	558	Amini *et al.*[53]
$CoFe_2O_4$	428 (T_{50})	Chagas *et al.*[10]
$NiFe_2O_4$	573 (T_{44})	Fouad *et al.*[54]

From the above analysis, it became clear that the co-precipitation route can yield cobalt ferrite nanoparticles that are highly active CO oxidation catalysts. A careful microstructural analysis revealed that this high activity is likely related to an easily overlooked nanocrystalline phase. Often, the PXRD analysis is used without paying much importance to the peak profiles. This can cause significant errors to the sample analysis.[12,23,24,26,28,38,43–47] It was shown that the synthesis pH is a suitable parameter to control the fraction of this nanocrystalline phase. The increased amount of nanocrystalline phase at pH 9 is advantageous for synthesizing samples with a very high surface area.

Conclusions

The constant pH precipitation method has been utilized for the preparation of a series of high surface area cobalt ferrite samples. Precipitation of cobalt ferrite without surfactant leads to the formation of samples with different amounts of crystalline and nanocrystalline contents. The relative amount of these contents can be controlled by variation of the pH during co-precipitation. The quantitative amounts of these crystalline and nanocrystalline contents can be estimated based on Rietveld refinement. TEM and SEM analysis further provide support for the two types of cobalt ferrite. Surface area, reducibility, and catalytic activity were dependent on the relative amount of these phases and were found to increase with the fraction of nanocrystalline cobalt ferrite in the samples. The best catalyst studied here was able to oxidize CO at room temperature.

Acknowledgements

We thank Prof. Robert Schlögl for providing the facility and opportunity to carry out this work. We thank, Dr Patric Cast for the catalytic measurement, Maike Hashagen (BET-SA), Gisela Weinberg (SEM), and Dr Julia Schumann (TPR).

References

1 G. Maniak, P. Stelmachowski, J. J. Stanek, A. Kotarba and Z. Sojka, *Catal. Commun.*, 2011, **15**, 127–131.
2 R. Galindo, S. Gutiérrez, N. Menéndez and P. Herrasti, *J. Alloys Compd.*, 2014, **586**, 1–5.
3 Z. Beji, M. Sun, L. S. Smiri, F. Herbst, C. Mangeney and S. Ammar, *RSC Adv.*, 2015, **5**, 65010–65022.
4 L. Menini, M. C. Pereira, L. A. Parreira, J. D. Fabris and E. V. Gusevskaya, *J. Catal.*, 2008, **254**, 355–364.
5 J. Smit and H. P. J. Wijn, *Ferrites: physical properties of ferrimagnetic oxides inrelation to their technical applications*, Philips' technical library, Eindhovan, 1959.
6 B. D. Cullity and C. D. Graham, *Introduction to Magnetic Materials*, John Wiley & Sons, Inc., Hoboken, New Jersey, 2009.
7 D. Li, H. Yun, B. T. Diroll, V. V. T. Doan-Nguyen, J. M. Kikkawa and C. B. Murray, *Chem. Mater.*, 2016, **28**, 480–489.
8 A. Indra, P. W. Menezes, N. R. Sahraie, A. Bergmann, C. Das, M. Tallarida, D. Schmeißer, P. Strasser and M. Driess, *J. Am. Chem. Soc.*, 2014, **136**, 17530–17536.
9 M. I. Godinho, M. A. Catarino, M. I. da Silva Pereira, M. H. Mendonça and F. M. Costa, *Electrochim. Acta*, 2002, **47**, 4307–4314.
10 C. A. Chagas, E. F. de Souza, M. C. N. A. de Carvalho, R. L. Martins and M. Schmal, *Appl. Catal., A*, 2016, **519**, 139–145.
11 Y. Fu, H. Chen, X. Sun and X. Wang, *Appl. Catal., B*, 2012, **111**, 280–287.
12 M. Houshiar, F. Zebhi, Z. J. Razi, A. Alidoust and Z. Askari, *J. Magn. Magn. Mater.*, 2014, **371**, 43–48.
13 I. Sharifi, H. Shokrollahi, M. M. Doroodmand and R. Safi, *J. Magn. Magn. Mater.*, 2012, **324**, 1854.
14 N. C. Pramanik, T. Fujii, M. Nakanishi and J. Takada, *J. Mater. Chem.*, 2004, **14**, 3328.
15 Y. Zhang, Y. Liu, Z. Yang, R. Xiong and J. Shi, *J. Nanopart. Res.*, 2011, **13**, 4557–4563.
16 A. J. A. Rondinone, A. C. S. Samia and Z. J. Zhang, *J. Phys. Chem. B*, 1999, **103**, 6876–6880.
17 P. Puliová, J. Kováč, A. Voigt, P. Raschman, P. Pulišová, J. Kováč, A. Voigt and P. Raschman, *J. Magn. Magn. Mater.*, 2013, **341**, 93–99.
18 D. Hong, Y. Yamada, M. Sheehan, S. Shikano, C. H. Kuo, M. Tian, C. K. Tsung and S. Fukuzumi, *ACS Sustainable Chem. Eng.*, 2014, **2**, 2588–2594.
19 K. V. P. M. Shafi, A. Gedanken, R. Prozorov and J. Balogh, *Chem. Mater.*, 1998, **10**, 3445–3450.
20 N. Bao, L. Shen, Y. Wang, P. Padhan and A. Gupta, *J. Am. Chem. Soc.*, 2007, **129**, 12374–12375.
21 F. Schüth, M. Hesse and K. K. Unger, *Handbook of Heterogeneous Catalysis*, Wiley-VCH Verlag GmbH & Co. KGaA, 2008.
22 T. L. Templeton, A. S. Arrott, A. E. Curzon, M. A. Gee, X. Z. Li, Y. Yoshida, P. J. Schurer and J. L. Lacombe, *J. Appl. Phys.*, 1993, **73**, 6728–6730.
23 M. Rajendran, R. C. Pullar, A. K. Bhattacharya, D. Das, S. N. Chintalapudib and C. K. Majumdar, *J. Magn. Magn. Mater.*, 2001, **232**, 71–83.
24 Y. Il Kim, D. Kim and C. S. Lee, *Phys. B*, 2003, **337**, 42–51.
25 S. Ayyappan, S. Mahadevan, P. Chandramohan, M. P. Srinivasan, J. Philip and B. Raj, *J. Phys. Chem. C*, 2010, **114**, 6334–6341.

26 P. C. Fannin, C. N. Marin, I. Malaescu, N. Stefu, P. Vlazan, S. Novaconi, P. Sfirloaga, S. Popescu and C. Couper, *Mater. Des.*, 2011, **32**, 1600–1604.
27 I. H. Gul, A. Maqsood, M. Naeem and M. N. Ashiq, *J. Alloys Compd.*, 2010, **507**, 201–206.
28 Y. Zhang, Z. Yang, D. Yin, Y. Liu, C. Fei, R. Xiong, J. Shi and G. Yan, *J. Magn. Magn. Mater.*, 2010, **322**, 3470–3475.
29 K. Maaz, A. Mumtaz, S. K. Hasanain and A. Ceylan, *J. Magn. Magn. Mater.*, 2007, **308**, 1–18.
30 M. Behrens, *Catal. Today*, 2015, **246**, 46–54.
31 J. Schumann, T. Lunkenbein, A. Tarasov, N. Thomas, R. Schlögl and M. Behrens, *ChemCatChem*, 2014, **6**, 2889–2897.
32 J. Schumann, A. Tarasov, N. Thomas, R. Schlögl and M. Behrens, *Appl. Catal., A*, 2016, **516**, 117–126.
33 J. C. Gonzalez, M. G. Gonzalez, M. A. Laborde and N. Moreno, *Appl. Catal.*, 1986, **20**, 3–13.
34 R. Brown, M. E. Cooper and D. A. Whan, *Appl. Catal.*, 1982, **3**, 177–186.
35 E. Manova, T. Tsoncheva, D. Paneva, I. Mitov, K. Tenchev and L. Petrov, *Appl. Catal., A*, 2004, **277**, 119–127.
36 M. V. C. Sastri, R. P. Viswanath and B. Viswanathan, *Int. J. Hydrogen Energy*, 1982, **7**, 951–955.
37 A. Urdă, A. Herraïz, Á. Rédey and I. C. Marcu, *Catal. Commun.*, 2009, **10**, 1651–1655.
38 G. A. El-Shobaky, A. M. Turky, N. Y. Mostafa and S. K. Mohamed, *J. Alloys Compd.*, 2010, **493**, 415–422.
39 J. Rouquerol, F. Rouquerol, P. Llewellyn, G. Maurin and K. S. W. Sing, *Adsorption by powders and porous solids: principles, methodology and applications*, Academic press, 2013.
40 K. S. W. Sing, D. H. Everett, R. a. W. Haul, L. Moscou, R. a. Pierotti, J. Rouquérol and T. Siemieniewska, *Pure Appl. Chem.*, 1982, **54**, 2201–2218.
41 S. Brunauer, P. H. Emmett and E. Teller, *J. Am. Chem. Soc.*, 1938, **60**, 309–319.
42 A. V Neimark, K. S. W. Sing and M. Thommes, *Handbook of Heterogeneous Catalysis*, Wiley-VCH Verlag GmbH & Co. KGaA, 2008.
43 M. M. Rashad, S. M. Mahmoud, Z. Abdel-Hamid, H. M. El-Sayed, A. E. Shalan, N. A. Khalifa and A. T. Kandil, *Part. Sci. Technol.*, 2016, DOI: 10.1080/02726351.2016.1239664.
44 S. Neveu, A. Bee, M. Robineau and D. Talbot, *J. Colloid Interface Sci.*, 2002, **255**, 293–298.
45 A. S. Albuquerque, M. V. C. Tolentino, J. D. Ardisson, F. C. C. Moura, R. De Mendona and W. A. A. MacEdo, *Ceram. Int.*, 2012, **38**, 2225–2231.
46 M. K. K. Shobana, H. Kwon and H. Choe, *J. Magn. Magn. Mater.*, 2012, **324**, 2245–2248.
47 Y. Qu, H. Yang, N. Yang, Y. Fan, H. Zhu and G. Zou, *Mater. Lett.*, 2006, **60**, 3548–3552.
48 H. Bao, X. Chen, J. Fang, Z. Jiang and W. Huang, *Catal. Lett.*, 2008, **125**, 160–167.
49 P. Mountapmbeme Kouotou, H. Vieker, Z. Y. Tian, P. H. Tchoua Ngamou, A. El Kasmi, A. Beyer, A. Gölzhäuser and K. Kohse-Höinghaus, *Catal. Sci. Technol.*, 2014, **4**, 3359.
50 Z. Y. Tian, H. Vieker, P. M. Kouotou and A. Beyer, *Faraday Discuss.*, 2015, **177**, 249–262.
51 P. M. Kouotou and Z. Y. Tian, *Phys. Status Solidi A*, 2015, **212**, 1508–1513.
52 S. Lee, J. S. Kang, K. T. Leung, W. Lee, D. Kim, S. Han, W. Yoo, H. J. Yoon, K. Nam and Y. Sohn, *J. Ind. Eng. Chem.*, 2016, **43**, 69–77.
53 E. Amini, M. Rezaei and M. Sadeghinia, *Chin. J. Catal.*, 2013, **34**, 1762–1767.
54 O. A. Fouad, K. S. Abdel Halim and M. M. Rashad, *Top. Catal.*, 2008, **47**, 61–65.